

# Kinetics of CH + N<sub>2</sub> Revisited with Multireference Methods

Lawrence B. Harding\* and Stephen J. Klippenstein

Chemical Sciences and Engineering Division, Argonne National Laboratory, 9700 South Cass Avenue, Argonne, Illinois 60439

James A. Miller

Combustion Research Facility, Sandia National Laboratories, Livermore, California 94551-0969

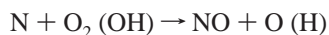
Received: September 18, 2007; In Final Form: October 26, 2007

The potential energy surface for the CH + N<sub>2</sub> reaction was reexamined with multireference ab initio electronic structure methods employing basis sets up to aug-cc-pvqz. Comparisons with related CCSD(T) calculations were also made. The multireference ab initio calculations indicate significant shortcomings in single reference based methods for two key rate-limiting transition states. Transition state theory calculations incorporating the revised best estimates for the transition state properties provide order of magnitude changes in the predicted rate coefficient in the temperature range of importance to the mechanism for prompt NO formation. At higher temperatures, two distinct pathways make a significant contribution to the kinetics. A key part of the transition state analysis involves a variable reaction coordinate transition state theory treatment for the formation of H + NCN from HNCN. The present predictions for the rate coefficients resolve the discrepancy between prior theory and very recent experimental measurements.

## 1. Introduction

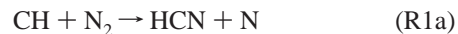
Prompt NO has fascinated combustion chemists for more than three decades. The phenomenon was first discovered by Fenimore<sup>1</sup> and reported at the Thirteenth International Combustion Symposium held in Salt Lake City in August of 1970. Fenimore's paper was the first one ever presented at a session of the Combustion Symposium organized around combustion-generated air pollution. His results were controversial from the beginning.

Fenimore was studying NO formation in the post-flame gases of a series of flames fueled by H<sub>2</sub>, CO, and various hydrocarbons at atmospheric and higher pressures. In his flames, the primary reaction zone, immediately adjacent to the burner surface, was largely unresolvable. Fenimore observed in all the flames that the NO increased with distance above the burner through the thermal, or Zeldovich, mechanism



However, the NO profiles extrapolated to zero at the burner surface in the H<sub>2</sub> and CO flames, whereas there was a non-zero intercept in all the hydrocarbon flames. This intercept NO, or prompt NO, increased with an increasing equivalence ratio up to about  $\Phi = 1.4$ , prompting Fenimore to attribute the phenomenon to a reaction in the primary reaction zone between a hydrocarbon free radical and molecular nitrogen, the products of which presumably react further to form NO.

Fenimore suggested two possibilities for the prompt- NO reaction



and



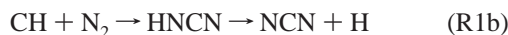
In 1970, both reactions (R1a and R2) were considered unlikely. R1a is spin-forbidden, and R2 is four-centered. There ensued a search for alternative explanations. The search was pursued by many people, and several other explanations were proposed.<sup>2–4</sup> However, in 1989, Miller and Bowman<sup>4</sup> examined the possible sources of prompt NO from a number of perspectives and concluded that indeed R1a must be responsible for the phenomenon, with perhaps a minor contribution at very high temperatures from the reaction of carbon atoms with N<sub>2</sub>



For a variety of reasons, direct experimental determinations of  $k_1$  have been limited to very high temperatures<sup>5,6</sup> ( $T > 2300$  K), although there have been some indirect inferences at lower temperatures.<sup>3,4,7</sup> At the same time, theoretical investigations of R1 have been hampered by the problem of handling the spin change in R1a, including finding the intersection that must occur between the doublet and the quartet potential energy surfaces and calculating the probability of a collision complex hopping from one surface to another. Many theorists have contributed to our understanding of these issues.<sup>8–17</sup> However, two investigations were pivotal. Cui et al.<sup>16</sup> showed conclusively that the spin-orbit coupling responsible for the spin flip in R1a was not strong enough to account for experimental observations. This

\* Corresponding author. E-mail: harding@anl.gov; fax: (630) 252-9292.

prompted Moskaleva et al.<sup>17,18</sup> to look for alternative product channels. They showed that indeed another set of products



could account for the experimental results available at the time, even though R1b is significantly endothermic. Subsequently, NCN has been detected in flames,<sup>19</sup> and photodissociation experiments on the HNCN<sup>20</sup> and DNCN radical<sup>21</sup> support the mechanism of Moskaleva and Lin. Additionally, a CASPT2 study has been reported<sup>22</sup> confirming the existence of the R1b pathway.

The controversy concerning R1 thus appeared to have been completely resolved<sup>15</sup> until very recently, when two independent studies called the results into question. A modeling study<sup>23</sup> of natural gas flames, using the rate calculated by Moskaleva and Lin, led to an underestimation, by more than a factor of 6, of the amount of prompt NO. Furthermore, Hanson and co-workers have extended the temperature range of their  $k_1(T)$  measurements to below 2000 K.<sup>24</sup> These measurements indicate that the Moskaleva and Lin prediction of the rate coefficient is an order of magnitude too low at 2000 K and probably even more so in the practically important temperature range, 1000 K <  $T$  < 2000 K. The present investigation was initiated to see if this discrepancy was due simply to an inadequacy of the theoretical methodology employed by Moskaleva and Lin or whether some new unidentified mechanism might be at work. Indeed, recently Berman et al.<sup>25</sup> have reported a new study of the potential surface suggesting that HNNC may play a role in the kinetics of this reaction.

In this paper, we extend the previous theoretical studies in several significant ways. Geometries and frequencies for all of the stationary points were obtained using a multireference method (CASPT2/aug-cc-pvtz). These calculations demonstrate that previous single reference approaches are inadequate for one of the key transition states. A second key extension of previous work is the use of variable reaction coordinate transition state theory to calculate the rate for the final dissociation of HNCN to H + NCN, a reaction for which there is no saddle point. Finally, we also briefly consider the possible contribution from the quartet state of CH.

## 2. Methods

**2.1. Electronic Structure Methods.** In this work, we made use of three ab initio electronic structure methods: (i) multireference second-order perturbation theory, CASPT2, (ii) internally contracted multireference configuration interaction with, CAS+1+2+QC, and without, CAS+1+2, the Davidson correction, and (iii) coupled-cluster theory restricted to single and double excitations with perturbative triple excitations, CCSD(T). All of the ab initio calculations employ the Dunning<sup>26–28</sup> correlation consistent basis sets. All of the multireference calculations and most of the CCSD(T) calculations were performed using the *MOLPRO* program package.<sup>29–34</sup> For comparison to previous work, we also report some CCSD(T) calculations performed with the *Gaussian 98* program.<sup>35</sup> The CASPT2 calculations can be performed either with or without internal contraction. For the largest active spaces, with no symmetry, it was only possible to perform the contracted CASPT2 calculations. For smaller active spaces and points of higher symmetry, the CASPT2 calculations were performed both ways. Note that the *Gaussian 98* and *MOLPRO* implementations of open shell CCSD(T) are different. The *MOLPRO* implementation uses ROHF orbitals, while *Gaussian 98* implementation

uses UHF orbitals. Again, for comparison to previous work, we also report some B3LYP calculations performed using *Gaussian 98*.

The final energies were extrapolated to a complete basis set (CBS) limit using the following formula<sup>36</sup>

$$E_{\text{aug-cc-pVxZ}} = E_{\text{CBS}} + \frac{B}{(n_x + 1)^4}$$

where  $n_T = 3$  and  $n_Q = 4$  for the aug-cc-pVTZ and aug-cc-pVQZ basis sets, respectively.

One of the prime motivations for this study was to characterize the key features of the potential surface using multireference ab initio methods. This problem is a challenging one for multireference approaches as a full valence active space, with 15 electrons in 13 orbitals, (15e,13o), is not computationally tractable. Takayanagi<sup>22</sup> reported a characterization of the surface using CASPT2 calculations with an (11e,11o) active space (this includes all valence orbitals except the nitrogen 2s orbitals) combined with a Shepard interpolation scheme for fitting the calculated points and deriving geometries and frequencies. In this work, we also use CASPT2 calculations to derive geometries and frequencies; however, we make use of analytic gradients<sup>37</sup> rather than Shepard interpolation. The majority of the calculations was performed using (3e,3o), (5e,5o), and/or (7e,7o) active spaces, although some key parts of the surface were reexamined with (9e,9o) and (11e,11o) active spaces to verify convergence with respect to the size of the active space. Geometry optimizations and frequency calculations were performed using the aug-cc-pvtz basis set. Single point CASPT2, CAS+1+2+QC, and CCSD(T) calculations were then performed using the larger aug-cc-pvqz basis set.

**2.2. Kinetics Methods.** The number of available states for all of the transition states was determined at the energy  $E$  and total angular momentum  $J$  resolved level. These transition state theory (TST) calculations were based on rigid-rotor harmonic-oscillator (RRHO) assumptions for the energy levels, except for the transition state connecting HNCN with H + NCN. For the latter transition state, the reverse reaction is a barrierless radical-radical reaction, for which RRHO assumptions are not expected to be appropriate. Thus, for that channel, the number of available states was instead obtained from variable reaction coordinate TST (VRC-TST).<sup>38–40</sup> Variational effects were also considered for TS<sub>1</sub> and TS<sub>3</sub> via standard reaction path evaluations but were found to be insignificant. The canonical partition function for the reactants was similarly determined with RRHO assumptions.

The rovibrational properties for the TST calculations were obtained from the CASPT2/aug-cc-pvtz calculations. The active spaces employed in these analyses are described in detail in the electronic structure results. The saddle point energies were obtained from the present best estimates, which are based on extrapolations of CCSD(T) or CI+1+2+QC calculations (as appropriate) with the aug-cc-pvtz and aug-cc-pvqz basis sets. The potential energy surface for the VRC-TST calculations in the NCN + H channel was obtained from an analytic fit to a grid of CI+1+2+QC/aug-cc-pvtz calculations. Essentially, identical results could be expected for a CASPT2 surface. These VRC-TST calculations are closely analogous to our prior calculations for the isoelectronic <sup>3</sup>HCCCH + H system described in detail in ref 41. An empirical dynamical correction factor of 0.9 is also incorporated as discussed previously.<sup>42</sup>

At low temperatures, stabilization to HCNN dominates the kinetics observed in a number of experimental studies.<sup>43–46</sup> This

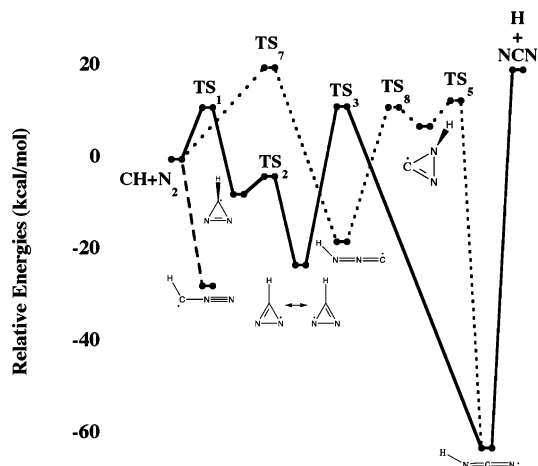
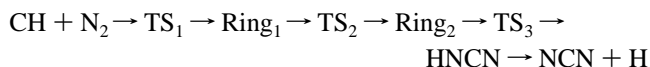


**Figure 1.** Schematic representation of the stationary point energies (including zero point) on the CH + N<sub>2</sub> doublet potential surface (see text for details).

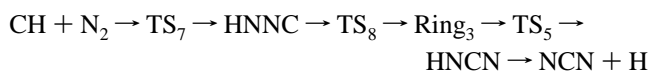
stabilization is irrelevant to the question of prompt NO, and so we do not consider this aspect further. At temperatures of 1000 K and higher, stabilization in this HCNN well becomes insignificant. For such temperatures, sample master equation simulations indicate that the rate coefficient to produce H + NCN is essentially independent of pressure. The HNCN well, which is the deepest well, is still not deep enough to support any collisional stabilization at such temperatures. In essence, the small number of vibrational modes (six) correlates with rapid dissociation and ineffective collisional stabilization. Thus, the results presented next are for the collisionless limit obtained with the methodology described in ref 47. The latter approach employs an analytic solution to the two-dimensional master equation based on the inversion of the rate matrix within the steady-state approximation. It requires only the canonical partition function for the reactants and the transition state number of available states for each of the transition states. It is readily implemented at the *E* and *J* resolved level.

### 3. Results and Discussion

**3.1. Electronic Structure Results.** *3.1.1. Overview.* A schematic representation of the important stationary points is given in Figure 1. Here, we use the transition state numbering scheme from ref 25, and we simplify the figure by omitting TS<sub>4</sub> and TS<sub>9</sub>, both of which are too high to be important in the thermal reaction. There are two distinct paths for the reaction CH + N<sub>2</sub> → NCN + H. Path A, first proposed by Moskaleva and Lin<sup>17</sup> and shown with a solid line in Figure 1, follows the route



Path B, proposed by Berman et al.,<sup>25</sup> is shown with a dotted line in Figure 1 and follows the route



The two paths converge at HNCN, which then dissociates to form the final products. There is a minor difference between path B as shown in Figure 1 and the results of Berman et al. Our results indicate that TS<sub>7</sub> connects directly to the reactants, while Berman et al. has TS<sub>7</sub> connected to Ring<sub>2</sub>. This may simply be a difference between the topology of the CCSD(T)

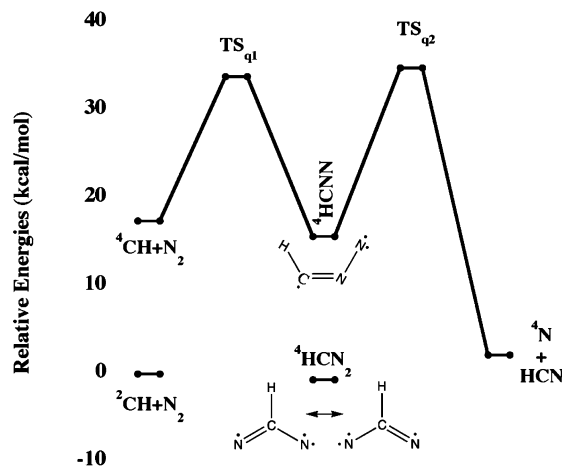


**Figure 2.** Schematic representation of the stationary point energies (including zero point) on the CH + N<sub>2</sub> quartet potential surface (see text for details).

**TABLE 1: CASPT2/aug-cc-pvtz Frequencies (cm<sup>-1</sup>) and Rotational Constants (GHz)**

	<i>N</i> <sub>act</sub> <sup>a</sup>	A	B	C	$\omega_1$	$\omega_2$	$\omega_3$	$\omega_4$	$\omega_5$	$\omega_6$
<sup>2</sup> CH	3		438.0		2945					
<sup>4</sup> CH	3				3134					
<sup>1</sup> N <sub>2</sub>	4		59.2		2328					
<sup>2</sup> Ring <sub>1</sub>	3	43.0	29.7	18.3	3186	1546	1102	1050	953	666
<sup>2</sup> Ring <sub>2</sub>	5	41.5	28.1	16.8	3286	1588	1225	902	891	625
<sup>2</sup> Ring <sub>3</sub>	5	42.1	30.1	18.0	3537	1482	1064	1003	786	492
<sup>2</sup> HCNN	7	606.2	12.1	11.9	3216	1839	1232	902	504	464
<sup>2</sup> HNNC	5	570.2	12.0	11.7	3417	1931	1368	1111	363	317
<sup>2</sup> HNCN	5	632.9	11.1	10.9	3505	1862	1186	1072	455	447
<sup>2</sup> HNC <sub>2</sub>	11	317.1	11.1	10.7	2739	1493	1063	794	458	226
<sup>4</sup> HCNN	7	108.4	14.4	12.7	3147	1336	1214	1035	713	512
<sup>4</sup> HNC <sub>2</sub>	5	95.6	13.1	11.5	3042	1266	1222	1139	807	550
<sup>3</sup> NCN	6		11.8		1623	1236	420	420		
<sup>1</sup> HCN	4		44.1		3490	2109	654	654		
<sup>2</sup> TS <sub>1</sub>	7	50.8	21.6	15.3	3156	1636	962	689	459	386 <i>i</i>
<sup>2</sup> TS <sub>2</sub>	5	42.7	29.6	17.9	3272	1512	1057	906	816	1188 <i>i</i>
<sup>2</sup> TS <sub>3</sub> -C <sub>2v</sub>	11	185.9	11.3	10.7	2892	1184	1036	952	580	243 <i>i</i>
<sup>2</sup> TS <sub>3</sub> -C <sub>s</sub>	11	334.2	11.1	10.7	2726	1451	1073	449	294	937 <i>i</i>
<sup>2</sup> TS <sub>5</sub>	5	53.8	19.3	14.2	3267	1680	1202	798	278	584 <i>i</i>
<sup>2</sup> TS <sub>7</sub>	5	45.9	25.4	16.4	2353	1518	978	952	726	1088 <i>i</i>
<sup>2</sup> TS <sub>8</sub>	5	56.5	20.2	15.2	3448	1701	1288	731	427	446 <i>i</i>
<sup>4</sup> TS <sub>q1</sub>	7	114.5	10.0	9.2	3097	1957	545	385	367	648 <i>i</i>
<sup>4</sup> TS <sub>q2</sub>	7	75.5	11.7	10.2	3313	1753	790	757	373	772 <i>i</i>

<sup>a</sup> *N*<sub>act</sub> is the number of orbitals (and electrons) included in the active space.

and CASPT2 surfaces, but it is unlikely to have a significant impact on the kinetics. A third path exists that begins with a barrierless addition to form HCNN, but subsequent barriers on this path have been shown<sup>11</sup> to be too high for it to compete with the first two paths. At higher temperatures, where the <sup>4</sup>Σ state of CH becomes thermally populated, reaction can also occur on the quartet surface as shown in Figure 2.

The rotational constants and vibrational frequencies for all of the stationary points shown in Figures 1 and 2 (and used in the kinetics calculations) are given in Table 1. One of the challenges in this study is the choice of active spaces used in the multireference calculations. Taking Ring<sub>1</sub> as an illustrative example, the structure is believed to be of C<sub>s</sub> symmetry. CASPT2 calculations with (3e,3o) or (9e,9o) active spaces yield a C<sub>s</sub> structure. Calculations with (5e,5o) or (7e,7o) active spaces, however, yield a slightly distorted C<sub>1</sub> structure owing to an imbalance between the orbitals included in the active space and those treated as closed shells. For Ring<sub>1</sub>, the differences in the structures and frequencies from the use of these four different active spaces are too small to be of significance in the kinetics

**TABLE 2: Relative Energies (kcal/mol) and  $T_1$  Diagnostics of Stationary Points from aug-cc-pvqz Calculations<sup>a</sup>**

	CASPT2 <sup>b</sup>	CASPT2 <sup>c</sup>	CAS+1+2+QC	CCSD(T)	$T_1$
<sup>2</sup> CH + N <sub>2</sub>	0.0(0.0)	0.0(0.0)	0.0(0.0)	0.0(0.0)	0.012
<sup>4</sup> CH + N <sub>2</sub>	13.9(13.1)	14.6(13.8)	17.4(16.8)	16.8(16.3)	0.016
<sup>2</sup> Ring <sub>1</sub>	-12.9(-11.8)			-12.2(-11.1)	0.014
<sup>2</sup> Ring <sub>2</sub>	-31.4(-30.4)	-31.9(-30.9)	-27.2(-26.3)	-27.6(-26.6)	0.015
<sup>2</sup> Ring <sub>3</sub>	0.4(1.6)			2.8(4.0)	0.014
<sup>2</sup> HCNN	-36.4(-35.3)			-31.7(-30.5)	0.040
<sup>2</sup> HNNC	-28.6(-27.6)	(-28.3)		-22.5(-26.4)	0.025
<sup>2</sup> HNCN	-70.1(-69.1)	(-69.6)		-67.4(-66.3)	0.020
<sup>2</sup> HCN <sub>2</sub>	2.7(3.1)	2.1(2.5)	9.3(9.4)	10.4(10.7)	0.023
<sup>2</sup> H + <sup>3</sup> NCN	14.6(14.4)	14.0(13.8)	21.1(21.0)	21.7(21.7)	0.013
<sup>4</sup> HCNN	4.4(4.7)			12.1(12.5)	0.029
<sup>4</sup> HCN <sub>2</sub>	-12.6(-12.9)	-13.2(-13.6)	-4.9(-5.4)	-4.9(-5.2)	0.021
<sup>1</sup> HCN + <sup>4</sup> N	-5.7(-7.1)	-6.3(-7.7)	-0.5(-2.0)	-1.2(-2.6)	0.012
<sup>2</sup> TS <sub>1</sub>	4.3(4.8)			8.9(9.5)	0.029
<sup>2</sup> TS <sub>2</sub>	-11.1(-10.1)			-7.0(-5.9)	0.048
<sup>2</sup> TS <sub>3</sub> -C <sub>s</sub>	2.8(3.2)	(2.7)	(9.0)	9.8(10.2)	0.034
<sup>2</sup> TS <sub>3</sub> -C <sub>2v</sub>	3.4(3.4)	2.8(2.8)	10.9(10.7)	-11.2(-15.2) <sup>d</sup>	0.063 <sup>d</sup>
				13.8(13.6) <sup>e</sup>	0.027 <sup>e</sup>
<sup>2</sup> TS <sub>5</sub>	7.7(8.3)	(6.9)	(10.0)	10.0(10.6)	0.041
<sup>2</sup> TS <sub>7</sub>	14.3(15.0)	(13.7)	(18.7)	18.2(18.9)	0.027
<sup>2</sup> TS <sub>8</sub>	5.0(5.7)			8.0(8.8)	0.024
<sup>4</sup> TS <sub>q1</sub>	27.5(27.0)			32.1(31.8)	0.023
<sup>4</sup> TS <sub>q2</sub>	24.6(23.6)			31.7(30.7)	0.027

<sup>a</sup> Numbers in parentheses are from aug-cc-pvtz calculations. The multireference calculations all employ an (11e,11o) active space. Geometries are all from caspt2/aug-cc-pvtz calculations. <sup>b</sup> Internally contracted. <sup>c</sup> Uncontracted. <sup>d</sup> On the basis of RHF configuration a. <sup>e</sup> On the basis of RHF configuration b.

calculations. For example, the largest difference in vibrational frequencies is less than 20 cm<sup>-1</sup>. Larger differences in frequencies and geometries with different active spaces are found for TS<sub>3</sub> (see section 3.1.3.).

The relative energies of the stationary points from (11e,11o)-CASPT2, (11e,11o)-CAS+1+2+QC, and CCSD(T) calculations are given in Table 2. Also given in Table 2 are the  $T_1$  diagnostics<sup>48</sup> from the CCSD(T) calculations. There is very good agreement between the CAS+1+2+QC and the CCSD(T) energies for all stationary points having a small  $T_1$  diagnostic (<0.02). The agreement between the CASPT2 energies and the CAS+1+2+QC and CCSD(T) energies is in general poor, although energies of similar structures are predicted quite accurately with CASPT2. For example, the relative energies of <sup>2</sup>HCN<sub>2</sub> and <sup>4</sup>HCN<sub>2</sub> are calculated to be 15.3, 14.2, and 15.3 kcal/mol using CASPT2, CAS+1+2+QC, and CCSD(T), respectively. However, the calculated energies of <sup>2</sup>HCN<sub>2</sub> relative to reactants are 2.7, 9.3, and 10.4 kcal/mol again for CASPT2, CAS+1+2+QC, and CCSD(T).

The relative energies of the stationary points used in the kinetics calculations are summarized in Table 3. In all cases except for TS<sub>3</sub>, these energies are obtained from CCSD(T)/CBS calculations at the CASPT2/aug-cc-pvtz geometries. For TS<sub>3</sub>, the CCSD(T) calculation was found to have a large  $T_1$  diagnostic,<sup>48</sup> and for this reason, the relative energy of TS<sub>3</sub> was determined using multireference calculations as described in section 3.1.3.

The three parts of the potential that have the most influence on the kinetics of this reaction are TS<sub>1</sub>, TS<sub>3</sub>, and the HNCN → NCN + H bond dissociation potential. In the next three subsections, we present and discuss the results of the electronic structure calculations for each of these parts.

**3.1.2. TS<sub>1</sub>.** A search in the region of TS<sub>1</sub> using (7e,7o)-CASPT2/aug-cc-pvtz calculations yielded two transition states and a minimum. The structures are shown in Figure 3. The structure labeled TS<sub>1</sub> is quite similar to the TS<sub>1</sub> structure in ref 18. The stationary point structures labeled TS<sub>0</sub> and Int<sub>0</sub>, however, were not found in the earlier study. The three structures have energies (relative to CH + N<sub>2</sub>) of 6.5, 3.1, and 3.1 kcal/mol.

**TABLE 3: Relative Energies Including Zero Point Corrections (kcal/mol) of Stationary Points**

	this work	G2M(RCC2) <sup>a</sup>	CCSD(T) <sup>b</sup>
<sup>2</sup> CH + N <sub>2</sub>	0.0	0.0	0.0
<sup>4</sup> CH + N <sub>2</sub>	17.45		
<sup>2</sup> Ring <sub>1</sub>	-8.34	-9.8	-8.8
<sup>2</sup> Ring <sub>2</sub>	-23.64	-23.5	-24.6
<sup>2</sup> Ring <sub>3</sub>	6.35	4.5	5.9
<sup>2</sup> HCNN	-28.34	-27.8	-29.6
<sup>2</sup> HNNC	-23.68		-25.1
<sup>2</sup> HNCN	-63.56	-61.1	-65.0
<sup>2</sup> HCN <sub>2</sub>	12.1		
<sup>2</sup> H + <sup>3</sup> NCN	19.54	21.5	17.8
<sup>4</sup> HCNN	15.68		
<sup>4</sup> HCN <sub>2</sub>	-0.66		
<sup>1</sup> HCN + <sup>4</sup> N	2.17		
<sup>2</sup> TS <sub>1</sub>	10.88	12.2	9.9
<sup>2</sup> TS <sub>2</sub>	-4.49	-4.8	-5.0
<sup>2</sup> TS <sub>3</sub> -C <sub>s</sub>	11.0	11.7	14.4
<sup>2</sup> TS <sub>3</sub> -C <sub>2v</sub>	12.9		
<sup>2</sup> TS <sub>5</sub>	12.46	15.8	11.6
<sup>2</sup> TS <sub>7</sub>	19.50		20.0
<sup>2</sup> TS <sub>8</sub>	10.81		14.5
<sup>4</sup> TS <sub>q1</sub>	33.88		
<sup>4</sup> TS <sub>q2</sub>	34.87		

<sup>a</sup> Ref 18. <sup>b</sup> Ref 25.

The new stationary points are found in CASPT2 calculations using (5e,5o), (7e,7o), and (9e,9o) active spaces and with cc-pvdz, aug-cc-pvdz, cc-pvtz, and aug-cc-pvtz basis sets. However, the new stationary points are not found in any CAS+1+2+QC, CCSD(T), or B3LYP optimizations. As a

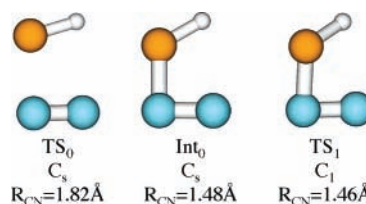


**Figure 3.** Stationary point structures along the reaction path between reactants and Ring<sub>1</sub> from (7e,7o)-CASPT2/aug-cc-pvtz calculations.

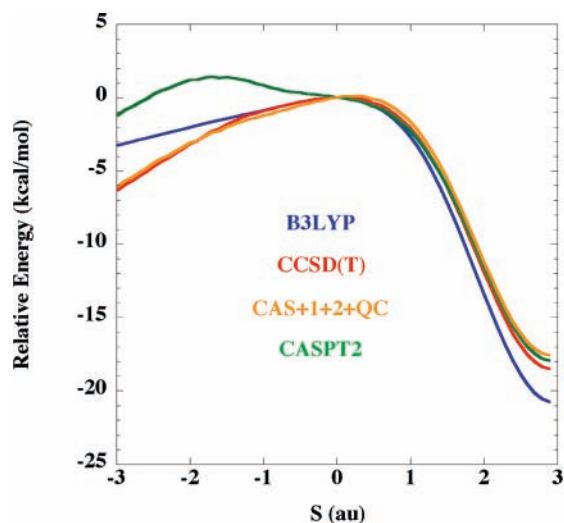
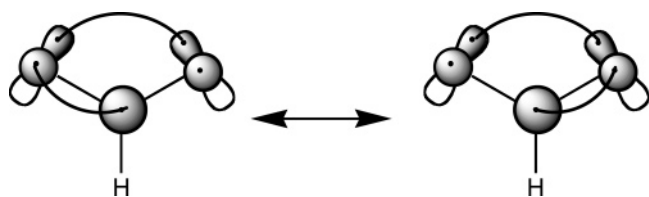


**Figure 4.** B3LYP, CCSD(T), CAS+1+2+QC, and CASPT2 energies along the B3LYP/6-311G(d,p) IRC for TS<sub>1</sub>. All energies are shifted to be zero at the transition state geometry,  $s = 0$ .  $s < 0$  corresponds to motion toward CH + N<sub>2</sub> and  $s > 0$  to motion toward Ring<sub>1</sub>.

further check on the calculations in this part of the potential surface, we followed the intrinsic reaction coordinate (IRC) from TS<sub>1</sub> using B3LYP and then evaluated CASPT2, CAS+1+2+QC, and CCSD(T) energies using the geometries from the B3LYP IRC. The results are shown in Figure 4. Again, it is seen that on the reactant side of TS<sub>1</sub>, the CASPT2 energies are anomalous. We tentatively conclude that the new stationary points, TS<sub>0</sub> and Int<sub>0</sub>, are artifacts of the CASPT2 calculations of unknown origin.

Focusing now on TS<sub>1</sub>, the structures and frequencies for TS<sub>1</sub> from a variety of electronic structure calculations are given in Table 4. All are found to be in good agreement with each other except for MP2, which gives an unrealistically high NN stretching frequency of 3211 cm<sup>-1</sup>. In the kinetics calculations, we use the structure and frequencies from the (7e,7o)-CASPT2/aug-cc-pvtz calculation.

**3.1.3. TS<sub>3</sub>.** Qualitatively, the electronic structure of TS<sub>3</sub> can be diagrammed as follows: having an essentially broken NN  $\sigma$



bond and a three electron allylic resonance in the  $\pi$  system. Both the broken  $\sigma$  bond and the resonance provide challenges to the electronic structure theory. In terms of orbitals, the

diagram translates into two dominant configurations of roughly equal weight

$$1a_1^2 2a_1^2 3a_1^2 4a_1^2 5a_1^2 1b_1^2 1b_2^2 2b_2^2 3b_2^2 6a_1^2 1a_2^1 \text{ (a)}$$

$$1a_1^2 2a_1^2 3a_1^2 4a_1^2 5a_1^2 1b_1^2 1b_2^2 2b_2^2 3b_2^2 4b_2^2 1a_2^1 \text{ (b)}$$

The two configurations differ by a double excitation between the 6a<sub>1</sub> and the 4b<sub>2</sub> orbitals. These two configurations are needed to allow the NN  $\sigma$  bond to evolve smoothly from a highly overlapping pair of bonding orbitals to a weakly overlapping pair of radical orbitals. As one moves down the reaction path toward Ring<sub>2</sub>, configuration a becomes increasingly dominant, while motion in the opposite direction causes configuration b to become increasingly dominant. For Ring<sub>2</sub>, the coefficients of configurations a and b are 0.94 and -0.14, respectively, while at TS<sub>3</sub>, these coefficients become 0.52 and -0.77, respectively. The next most important configurations are the ones describing the allylic resonance (c and d)

$$1a_1^2 2a_1^2 3a_1^2 4a_1^2 5a_1^2 1b_2^2 2b_2^2 3b_2^2 6a_1^2 1b_1^2 1a_2^1 \text{ (c)}$$

$$1a_1^2 2a_1^2 3a_1^2 4a_1^2 5a_1^2 1b_2^2 2b_2^2 3b_2^2 4b_2^2 1b_1^2 1a_2^1 \text{ (d)}$$

corresponding to a single excitation between the 1b<sub>1</sub> and the 2b<sub>1</sub> orbitals from configurations a and b. At Ring<sub>2</sub>, c has a coefficient of 0.15, while at TS<sub>3</sub>, c and d have coefficients of 0.13 and 0.15, respectively.

We find that the geometry of TS<sub>3</sub> depends dramatically on the electronic structure method used. To better understand as to why this is the case, we show, in Figure 5, some two-dimensional contour plots of the PES in the vicinity of TS<sub>3</sub>. These plots were obtained with both CASPT2 and CAS+1+2+QC calculations and with both aug-cc-pvdz and aug-cc-pvtz basis sets employing a (5e,5o) active space in each case. Two points are worth noting: first, the CASPT2 and CAS+1+2+QC calculations yield potentials that look remarkably similar. Second, all calculations show a potential that is very flat near TS<sub>3</sub>. This flatness is what causes the sensitivity of the exact location of the saddle points to the details of the electronic structure method used. Two saddle points can be seen in each of the four PESs shown in Figure 5. In the aug-cc-pvdz calculations, the two saddle points are of C<sub>s</sub> symmetry, lying slightly off the C<sub>2v</sub> axis, and are related to each other by symmetry. In the aug-cc-pvtz calculations, both saddle points lie on the C<sub>2v</sub> axis, one being the transition state for ring opening and (1,2)-hydrogen migration (TS<sub>3</sub>), and the second slightly lower saddle point being a transition state for (1,3)-hydrogen migration in HNCN. Because HNCN is of lower symmetry than Ring<sub>2</sub>, the reaction path for Ring<sub>2</sub> → HNCN must contain a

**TABLE 4: Geometries and Vibrational Frequencies for <sup>2</sup>TS<sub>1</sub>**

method	R <sub>CH</sub> (Å)	R <sub>CN</sub> (Å)	R <sub>NN</sub> (Å)	HCN angle (deg)	CNN angle (deg)	HCNN dihedral angle (deg)	$\omega_i$ (cm <sup>-1</sup> )
(7e,7o)-CASPT2/aug-cc-pvdz	1.104	1.485	1.222	122.3	86.1	31.8	3146, 1634, 978, 678, 496, 381 <i>i</i>
(7e,7o)-CAS+1+2/aug-cc-pvdz	1.103	1.486	1.212	121.4	88.3	22.7	3158, 1678, 977, 642, 448, 255 <i>i</i>
(7e,7o)-CAS+1+2+QC/aug-cc-pvdz	1.109	1.524	1.209	119.7	85.8	34.0	3096, 1696, 989, 633, 426, 370 <i>i</i>
(7e,7o)-CASPT2/aug-cc-pvtz	1.109	1.465	1.209	123.4	86.4	26.5	3156, 1636, 962, 689, 459, 386 <i>i</i>
B3LYP/6-311G(d,p) <sup>a</sup>	1.103	1.572	1.162	115.1	86.2	30.7	3000, 1900, 1037, 600, 301, 346 <i>i</i>
MP2/6-311G(d,p)	1.104	1.679	1.156	111.9	80.5	38.0	3211, 3057, 1279, 704, 500, 549 <i>i</i>
CCSD(T)/aug-cc-pvdz	1.115	1.560	1.197	116.5	86.3	31.3	3032, 1745, 1002, 597, 388, 294 <i>i</i>
CCSD(T)/aug-cc-pvtz <sup>b</sup>	1.096	1.535	1.173				

<sup>a</sup> Ref 18. <sup>b</sup> Ref 25.

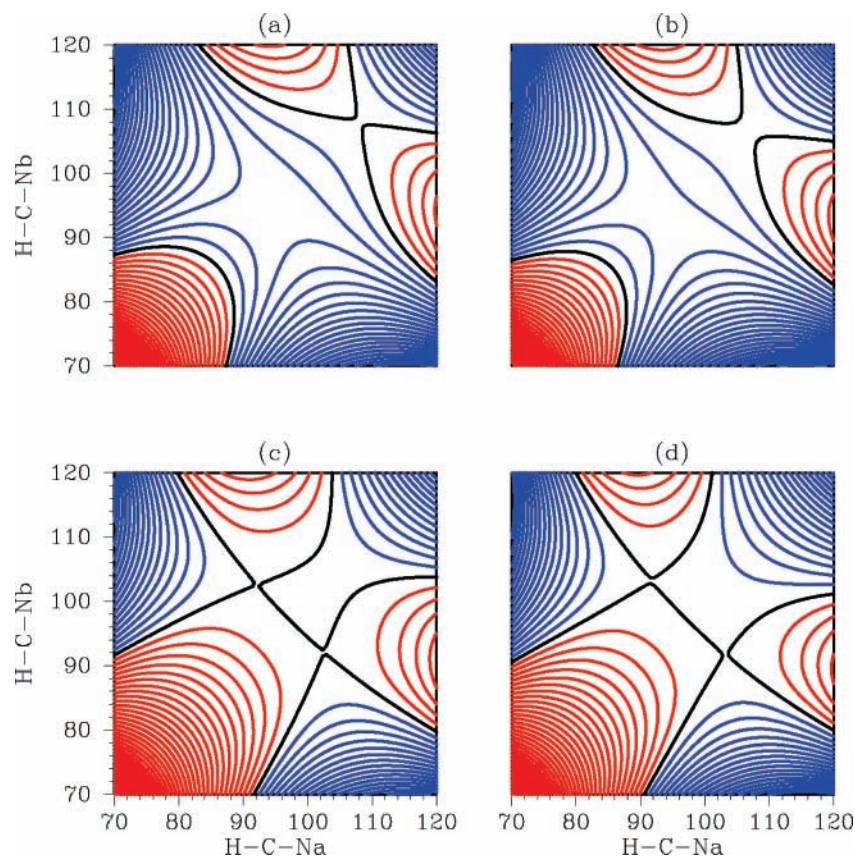


**Figure 5.** Contour plots of the potential surface in the vicinity of TS<sub>3</sub> as a function of the two HCN angles. The remaining degrees of freedom are optimized at each point using CASPT2. The contour increment is 0.5 kcal/mol. The blue contours represent energies below that of TS<sub>3</sub>, the red contours represent energies above that of TS<sub>3</sub>, and the black contours correspond to the energy of TS<sub>3</sub>. (a) CASPT2/aug-cc-pvtz, (b) CAS+1+2+QC/aug-cc-pvtz, (c) CASPT2/aug-cc-pvdz, and (d) CAS+1+2+QC/aug-cc-pvdz.

**TABLE 5: Geometries and Vibrational Frequencies for TS<sub>3</sub> from Multireference Calculations<sup>a</sup>**

method	$R_{\text{CH}}$ (Å)	$R_{\text{CN}_a}$ (Å)	$R_{\text{CN}_b}$ (Å)	HCN <sub>a</sub> angle (deg)	HCN <sub>b</sub> angle (deg)	$\omega_i$ (cm <sup>-1</sup> )	
(3e,3o)-CASPT2/aug-cc-pvdz	1.128	1.349	1.277	104.5	104.8	2904, 1474, 948, 850, 559, 554 <i>i</i>	
(5e,5o)-CASPT2/aug-cc-pvdz	1.148	1.305	1.292	92.1	102.5	2804, 1480, 1064, 470, 406, 459 <i>i</i>	
(5e,5o)-CAS+1+2+QC/aug-cc-pvdz	1.148	1.305	1.289	91.7	103.1	2790, 1399, 1058, 472, 423, 511 <i>i</i>	
(9e,9o)-CASPT2/aug-cc-pvdz	1.149	1.309	1.291	90.4	103.3	2803, 1407, 1045, 454, 423, 532 <i>i</i>	
(11e,11o)-CASPT2/aug-cc-pvdz	1.161	1.310	1.286	87.2	105.2	2705, 1395, 1043, 445, 384, 896 <i>i</i>	
(11e,11o)-CASPT2/cc-pvtz (from ref 22)	1.138	1.296	1.283	92.0	102.5	2508, 1504, 1092, 806, 269, 385 <i>i</i>	
(11e,11o)-CASPT2/cc-pvtz (this work)	1.147	1.287	1.274	89.0	100.8	2748, 1444, 1067, 459, 294, 902 <i>i</i>	
(5e,5o)-CASPT2/aug-cc-pvtz	1.108	1.309	1.309	108.0	108.0	2985, 1424, 1062, 1029, 656, 361 <i>i</i>	
(5e,5o)-CAS+1+2+QC/aug-cc-pvtz	1.111	1.306	1.306	106.6	106.6	2990, 1123, 1058, 1000, 639, 334 <i>i</i>	
(9e,9o)-CASPT2/aug-cc-pvtz	1.110	1.308	1.308	106.1	106.1	2968, 1176, 1039, 971, 606, 298 <i>i</i>	
	<sup>2</sup> TS <sub>3</sub> -C <sub>s</sub>	1.152	1.284	1.274	88.7	99.5	2726, 1451, 1073, 449, 294, 937 <i>i</i>
(11e,11o)-CASPT2/aug-cc-pvtz	<sup>2</sup> HCN <sub>2</sub>	1.146	1.282	1.282	95.2	95.2	2739, 1493, 1063, 794, 458, 226
	<sup>2</sup> TS <sub>3</sub> -C <sub>2v</sub>	1.120	1.305	1.305	104.7	104.7	2892, 1184, 1036, 952, 580, 243 <i>i</i>

<sup>a</sup> All structures are planar.

**TABLE 6: Geometries and Vibrational Frequencies for TS<sub>3</sub> from Single Reference Calculations<sup>a</sup>**

method	$R_{\text{CH}}$ (Å)	$R_{\text{CN}_a}$ (Å)	$R_{\text{CN}_b}$ (Å)	HCN <sub>a</sub> angle (deg)	HCN <sub>b</sub> angle (deg)	$\omega_i$ (cm <sup>-1</sup> )
UB3LYP/6-311G**	1.164	1.304	1.246	85.0	112.4	2502, 1494, 1060, 542, 509, 1212 <i>i</i>
UHF/6-311G**	1.213	1.287	1.250	68.4	131.8	2326, 1472, 1105, 483, 478, 2495 <i>i</i>
UMP2/6-311G**	1.197	1.368	1.198	77.5	119.0	2230, 1914, 852, 572, 531, 1688 <i>i</i>
CCSD(T)/aug-cc-pvtz <sup>b</sup>	1.142	1.300	1.254	91.0	106.1	
RCCSD(T)/aug-cc-pvdz	1.158	1.299	1.282	92.0	96.5	2729, 1625, 1097, 493, 364, 797 <i>i</i>

<sup>a</sup> All structures are planar. <sup>b</sup> Ref 25.

bifurcation. In the aug-cc-pvdz calculations, this bifurcation occurs between Ring<sub>2</sub> and TS<sub>3</sub>, while in the aug-cc-pvtz calculations, it occurs between TS<sub>3</sub> and HNCN.

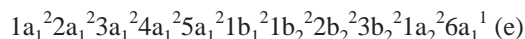
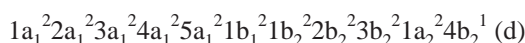
Geometries for TS<sub>3</sub> calculated with a number of different methods and basis sets are listed in Tables 5 and 6. All of the

structures are planar, but for the reasons discussed previously, some methods yield saddle points having C<sub>2v</sub> symmetry, while others yield structures having C<sub>s</sub> symmetry. Consider first the multireference calculations. In Table 5, results are shown for the (3e,3o), (5e,5o), (9e,9o), and (11e,11o) active spaces. The

active orbitals for the (3e,3o) calculation consist of  $6a_14b_21a_2$  (in  $C_{2v}$  symmetry). Note that this active space does not include configurations c or d describing the allylic resonance. When the  $C_{2v}$  symmetry restriction is relaxed in the (3e,3o)-CASSCF calculation, the wavefunction breaks symmetry by converging to either one of the two localized resonance structures shown previously. The minimum active space required to prevent this artificial symmetry breaking is a (5e,5o) space consisting of the following orbitals:  $6a_11b_2b_14b_21a_2$ . Note that a (7e,7o) active space is also found to undergo symmetry breaking (because one of the CN  $\sigma$  bond pairs is included in the active space and one is not), while the (9e,9o) and (11e,11o) active spaces do not undergo symmetry breaking. This analysis suggests that the (5e,5o), (9e,9o), and (11e,11o) active spaces all give qualitatively reasonable results, while the (3e,3o) and (7e,7o) active spaces suffer from symmetry breaking artifacts.

Also shown in Table 5 are comparisons of results obtained with three different basis sets, aug-cc-pvdz, cc-pvtz, and aug-cc-pvtz. The two smaller basis sets yield saddle point structures of  $C_s$  symmetry. The largest basis set, aug-cc-pvtz, is found to yield a transition state structure having  $C_{2v}$  symmetry. With the largest basis set, we also find a dependence on the size of the active space. With the (5e,5o) and (9e,9o) active spaces, we find a single saddle point of  $C_{2v}$  symmetry, while the (11e,11o) active space yields a shallow  $C_{2v}$  minimum corresponding to a ring-opened intermediate,  ${}^2\text{HCN}_2$ , a  $C_{2v}$  saddle point between  ${}^2\text{HCN}_2$  and Ring<sub>2</sub>, and two  $C_s$  symmetry saddle points between  ${}^2\text{HCN}_2$  and HNCN. The relative energies of  ${}^2\text{HCN}_2$ , TS<sub>3-C<sub>s</sub></sub> and TS<sub>3-C<sub>2v</sub></sub>, in this calculation are 0.00, 0.04, and 1.01 kcal/mol, respectively.

Consider now the TS<sub>3</sub> structures obtained from single reference calculations (Table 6). B3LYP, UHF, and UMP2 are all found to give structures very distorted from  $C_{2v}$  symmetry. The problem here is that the HF wavefunction yields a very poor description of the tri-radical character found in the multireference calculations. In fact, the two lowest RHF wavefunctions at the geometry of the (5e,5o)-CASPT2/aug-cc-pvtz saddle point are a  ${}^2B_2$  and a  ${}^2A_1$  state having the orbital occupancies shown in d and e



with four  $\pi$  electrons rather than three. The CCSD(T) calculation, when constrained to have three  $\pi$  electrons, yields a saddle point structure only slightly distorted from  $C_{2v}$  and in reasonable agreement with the structures from the multireference calculations. There is, however, an ambiguity in the CCSD(T) calculations at least when applied to  $C_{2v}$  geometries in that the calculations can be based on either configuration a or configuration b. In Figure 6, we plot the RHF and CCSD(T) energies and  $T_1$  diagnostics corresponding to configurations a and b along a  $C_{2v}$  constrained minimum energy path (MEP) for ring opening of Ring<sub>2</sub>. Both CCSD(T) calculations exhibit divergent behavior in the vicinity of TS<sub>3</sub>. In Figure 7, we plot the results of analogous UHF based calculations. The curves for configurations a and b are quite similar to those in Figure 6. Also shown in Figure 7 are calculations based on the lowest UHF solution at each point. In the vicinity of TS<sub>3</sub>, the lowest UHF solution is a highly spin contaminated  $A_1$  state ( $S^2 = 1.9$ ). The UHF wavefunction is found to undergo symmetry breaking quite close to the Ring<sub>2</sub> minimum.

Given the extreme sensitivity of the TS<sub>3</sub> structure to the electronic structure method used, none of the calculations shown

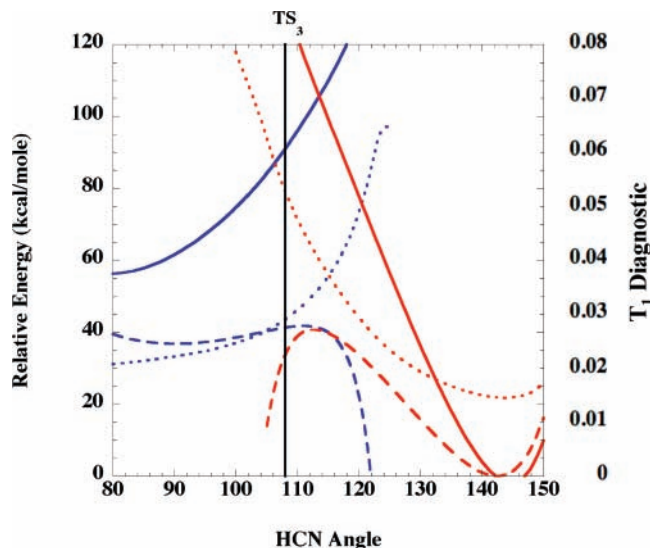


**Figure 6.** RHF and CCSD(T) energies and  $T_1$  diagnostics along a  $C_{2v}$  MEP for ring opening of Ring<sub>2</sub>. The geometries are obtained from  $C_{2v}$  constrained (5e,5o)-CASPT2/aug-cc-pvtz geometry optimizations. Solid lines are RHF energies, dashed lines are CCSD(T) energies, and dotted lines are the  $T_1$  diagnostics. The red curves correspond to configuration a and the blue to configuration b. The vertical black line denotes the position of TS<sub>3</sub> from the (5e,5o)-CASPT2/aug-cc-pvtz calculation.

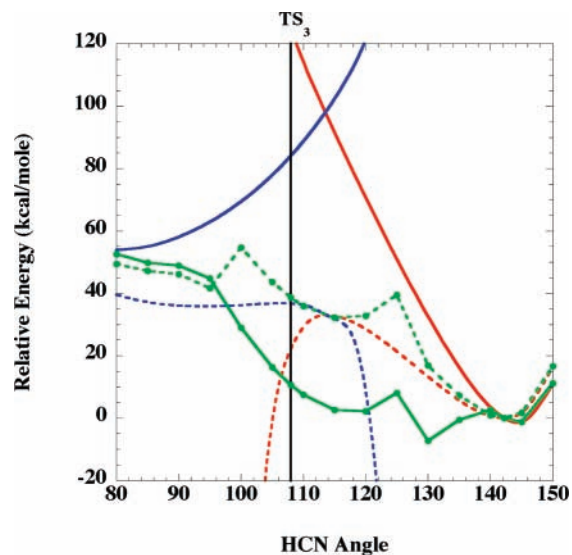


**Figure 7.** UHF and CCSD(T) energies along a  $C_{2v}$  MEP for ring opening of Ring<sub>2</sub>. The geometries are obtained from  $C_{2v}$  constrained (5e,5o)-CASPT2/aug-cc-pvtz geometry optimizations. Solid lines are UHF energies, and dashed lines are CCSD(T) energies. The red curves correspond to configuration a, the blue to configuration b, and the green to the lowest UHF solution. The vertical black line denotes the position of TS<sub>3</sub> from the (5e,5o)-CASPT2/aug-cc-pvtz calculation.

in Tables 5 and 6 can be considered to be definitive regarding the question of a  $C_{2v}$  or  $C_s$  saddle point. However, even if the actual saddle point is  $C_s$ , as in Figure 5c,d, variational effects in the transition state theory calculation will tend to shift the dynamical bottleneck off the saddle point, toward the  $C_{2v}$  axis and toward Ring<sub>2</sub>, where the reaction valley is more constrained (higher frequencies and lower reaction path degeneracy). For this reason, we now focus on determining the energy of TS<sub>3-C<sub>2v</sub></sub> as accurately as possible.

As noted in section 3.1.1., the energies of the stationary points (except for TS<sub>3</sub>) are calculated at the CCSD(T)/aug-cc-pvqz//CASPT2/aug-cc-pvtz level. For TS<sub>3</sub>, the above analysis and the large  $T_1$  diagnostic found in the CCSD(T)/aug-cc-pvqz//

**TABLE 7: Energy Estimates from Multireference aug-cc-pvqz Calculations for TS<sub>3</sub>-C<sub>2v</sub> (kcal/mol)<sup>a</sup>**

method	N <sub>act</sub>	scheme 1 (direct)	scheme 2 (via Ring <sub>2</sub> )	scheme 3 (via quartet)
CASPT2 <sup>b</sup>	11	2.8(2.8)	7.1(6.1)	11.1(11.4)
CASPT2 <sup>c</sup>	11	3.4(3.4)	7.2(6.2)	11.1(11.4)
CAS+1+2	11	14.3(14.0)	11.3(10.3)	11.9(12.1)
CAS+1+2+QC	11	10.9(10.7)	10.5(9.3)	10.9(11.2)
CASPT2 <sup>b</sup>	5		6.6(7.1)	10.3(10.6)
CAS+1+2	5		11.3(11.7)	11.5(11.8)
CAS+1+2+QC	5		11.1(10.8)	10.8(10.6)

<sup>a</sup> Numbers in parentheses were obtained using the aug-cc-pvtz basis set. <sup>b</sup> Uncontracted. <sup>c</sup> Contracted.

CASPT2/aug-cc-pvtz calculation (0.063 for configuration a and 0.027 for configuration b) suggest that the CCSD(T) calculation may not be reliable for this saddle point. We note that several other stationary points listed in Table 2 have unusually large  $T_1$  diagnostics (TS<sub>2</sub>, 0.048; TS<sub>5</sub>, 0.041; and HCN<sub>N</sub>, 0.040), but the kinetics is not sensitive to these three stationary points. We also note that the  $T_1$  diagnostic, having been developed for CCSD calculations, is not a rigorous indication of problems with the CCSD(T) calculations. However, as noted above, the CCSD(T) energies show clear evidence of divergent behavior in the vicinity of TS<sub>3</sub>, and for this reason, we choose to rely on multireference methods for estimating the energy and rovibrational properties of this saddle point.

Three schemes for calculating the energy of TS<sub>3</sub>-C<sub>2v</sub> relative to reactants were used: (i) direct multireference calculations of TS<sub>3</sub>-C<sub>2v</sub> relative to CH + N<sub>2</sub>, (ii) multireference calculation of TS<sub>3</sub>-C<sub>2v</sub> relative to Ring<sub>2</sub> combined with CCSD(T) calculation of Ring<sub>2</sub> relative to CH + N<sub>2</sub>, and (iii) multireference calculation of TS<sub>3</sub>-C<sub>2v</sub> relative to the quartet state, <sup>4</sup>HCN<sub>2</sub> (which lies close to TS<sub>3</sub>-C<sub>2v</sub>), combined with CCSD(T) calculation of the quartet relative to CH + N<sub>2</sub>. The results are summarized in Table 7. All calculations employ the (11e,11o)-CASPT2/aug-cc-pvtz C<sub>2v</sub> geometry for TS<sub>3</sub>-C<sub>2v</sub> given in Table 5. The single point calculations in Table 7 were all obtained using the aug-cc-pvqz basis set. The CASPT2 based estimates were found to vary from 2.8 to 11.1 kcal/mol depending on the scheme used and the size of the active space. The CAS+1+2+QC estimates show much smaller variations, ranging from 10.5 to 10.9 kcal/mol. In our kinetics calculations, we used a value of 10.9 kcal/mol (the average of the (11e,11o)-CAS+1+2+QC estimates extrapolated to the complete basis set limit). Inclusion of zero point corrections gives the result shown in Table 3 (12.9 kcal/mol).

It was not feasible to perform a (11e,11o)-CAS+1+2+QC/aug-cc-pvqz calculation for TS<sub>3</sub>-C<sub>s</sub>. Instead, we used the (11e,11o)-CASPT2/CBS calculation to fix the energy of TS<sub>3</sub>-C<sub>s</sub> relative to TS<sub>3</sub>-C<sub>2v</sub> (-1.0 kcal/mol, without zero point and -1.9 kcal/mol, including zero point). However, the kinetics calculations indicate that TS<sub>3</sub>-C<sub>s</sub> has no effect on the kinetics.

These energy estimates (11.0 kcal/mol for TS<sub>3</sub>-C<sub>s</sub> and 12.9 kcal/mol for TS<sub>3</sub>-C<sub>2v</sub>) are in good agreement with the earlier calculations of Moskaleva et al. (11.7 kcal/mol) and are in reasonable agreement with the results of Berman et al. (14.4 kcal/mol), although the geometry from the multireference calculations is very different from either of the earlier single reference calculations. Interestingly, our own CCSD(T) calculations (based on ROHF reference wavefunctions and the CASPT2 C<sub>2v</sub> geometry) yield energies of 12.2 or 17.7 kcal/mol depending on whether configuration a or b is used. The good agreement between the CCSD(T) calculation using configuration a and the multireference calculations must be considered as fortuitous

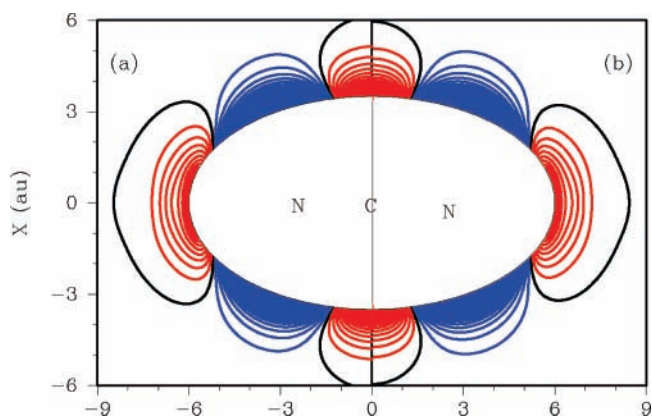


**Figure 8.** Contour plots of the H + NCN interaction potential. The NCN fragment is constrained to be collinear, and the plotting plane contains this molecular axis. The red contours denote positive energies, and the blue contours denote negative energies. Zero energy is defined to be the energy of the H + NCN asymptote. The contour increment is 1 kcal/mol. The blanked circle in the center hides parts of the surface that are not relevant to the association kinetics and were therefore not calculated. The left side (a) was calculated using (7e,7o)-CAS+1+2+QC/aug-cc-pvtz and the right side (b) with (7e,7o)-CASPT2/aug-cc-pvtz.

because, as seen in Figure 6, the CCSD(T) energy for configuration a is clearly beginning to diverge for this geometry.

**3.1.4. HNCN → NCN + H.** The final step, the dissociation of HNCN to H + NCN, is the reverse of a barrierless radical-radical addition. The rate of this reaction will be determined by the long-range interaction potential between the H atom and the NCN fragment. A two-dimensional contour plot of this interaction potential is shown in Figure 8. As expected, the plot shows barrierless paths for addition to either nitrogen atom. Note that the left side of this plot is calculated using multireference CI, while the right side was calculated with second order perturbation theory. The fact that the two sides of the plot are nearly identical demonstrates that the two multireference methods are in agreement with each other. NCN is formed in the ground, <sup>3</sup>Σ<sub>g</sub><sup>-</sup>, state. Consequently, the potential shown in Figure 8 is cylindrically symmetric, containing all the information needed for the variational transition state theory calculation.

In Figure 9, we show one-dimensional potential curves for this NH bond cleavage reaction using both multireference and single reference, CCSD(T), methods. For the CCSD(T) calculations, we show potential curves calculated using both UHF orbitals, as implemented in *Gaussian 98*, and ROHF orbitals, as implemented in *MOLPRO*. The ROHF-RCCSD(T) potential curve exhibits a spurious barrier to the reverse reaction, while the UHF-CCSD(T) calculations are significantly less attractive than the multireference calculations in the kinetically sensitive region,  $R_{\text{NH}} = 2-3$  Å. For example, at  $R_{\text{NH}} = 2.5$  Å, the UHF/CCSD(T), CASPT2, and CAS+1+2+QC interaction energies (relative to H + NCN) are -0.35, -1.2, and -1.1 kcal/mol, respectively. In this region, the UHF wavefunction is highly spin contaminated, having an  $S^2$  expectation value of 2.2 instead of the expected value for a pure doublet of 0.75. These results demonstrate, not unexpectedly, that CCSD(T) calculations are not appropriate for this part of the potential surface. See ref 49 for a recent review of the problems associated with using coupled-cluster theory for bond breaking reactions.

**3.2. Kinetics Results.** **3.2.1. Path A.** The present theoretical predictions for path A are illustrated in Figure 10. These predictions are for the collisionless limit of the rate coefficient for the CH + N<sub>2</sub> → H + NCN reaction. Included in the plot are the predictions obtained when considering each transition state individually, as well as the full calculation, which properly

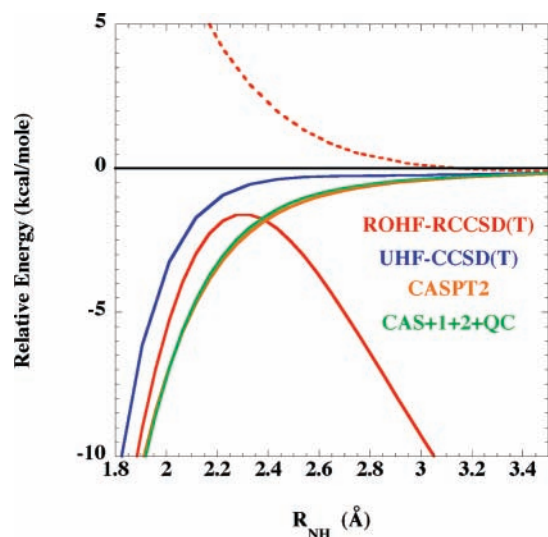


**Figure 9.** One-dimensional potential curves for  $\text{H} + \text{NCN} \rightarrow \text{HNCN}$ . The NCN radical is constrained to its equilibrium geometry. The HNC angle is fixed at  $100^\circ$ . All calculations employ the aug-cc-pvdz basis set. The solid lines are for the doublet state and the dashed line for the quartet state. The asymptotic energy for the ROHF-RCCSD(T) calculations is taken from the quartet state.

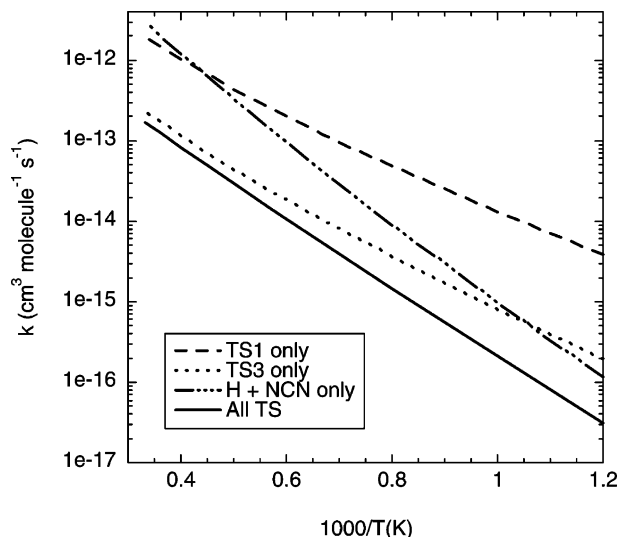


**Figure 10.** Plot of the predicted rate coefficient for  $\text{CH} + \text{N}_2 \rightarrow \text{NCN} + \text{H}$  via path A when considering different subsets of the transition states along the path.

incorporates the joint effect of each of the transition states. At low temperatures, the decomposition of HNCN to form  $\text{H} + \text{NCN}$  is clearly the rate-limiting step, while at higher temperature,  $\text{TS}_3$  provides the rate-limiting bottleneck. At intermediate temperatures (i.e., from about 500 to 1500 K), both transition states play an important role in the kinetics. The entrance channel transition state,  $\text{TS}_1$ , is never the dominant bottleneck, although it does yield a minor reduction in the rate coefficient at the highest temperatures. Notably, the implementation of the CCSD(T) properties for  $\text{TS}_3$  yields a rate constant that is 2 times larger at 2000 K.

**3.2.2. Path B.** The predicted temperature dependence of the rate coefficient for reaction via path B is illustrated in Figure 11, together with the corresponding results for path A and for a calculation in which both path A and path B are considered jointly. For path B,  $\text{TS}_7$ , the transition state for the initial addition to form HNCN, is the dominant bottleneck. The  $\text{TS}_7$  barrier energy of 19.5 kcal/mol is substantially greater than the

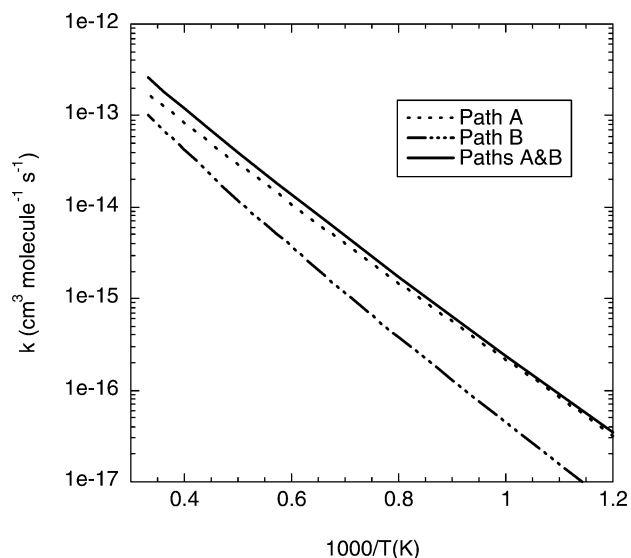


**Figure 11.** Plot of the contributions from different pathways to the predicted rate coefficient for  $\text{CH} + \text{N}_2 \rightarrow \text{NCN} + \text{H}$ .

corresponding maximum saddle point energy of 12.9 kcal/mol for path A. Thus, the contribution from path B increases with increasing temperature, with the ratio of the path B to path A rate coefficients varying from 0.21, to 0.41, to 0.60 as the temperature increases from 1000, to 2000, and then to 3000 K. The two contributions are not directly additive, and so the joint rate coefficient is increased by the slightly reduced factors of 1.13, 1.34, and 1.53 for these same temperatures.

**3.2.3.  $^4\text{CH} + \text{N}_2$ .** Another pathway that has not been considered previously involves the reaction on solely the quartet state. With this pathway, the spin crossing may be more efficient as it would arise through collision induced intersystem crossing of  $\text{CH}$  ( $^2\text{CH} + \text{M} \rightarrow ^4\text{CH} + \text{M}$ ). The quartet reaction proceeds via first the formation of a quartet HNCN complex, followed by NN fission to produce  $\text{HCN} + ^4\text{N}$ . The entrance and exit barriers for this pathway are both quite large, and both present significant bottlenecks to the reaction. At the CCSD(T)/CBS level, they are 33.9 and 34.9 kcal/mol, respectively, relative to  $^2\text{CH} + \text{N}_2$ . As a result, the predicted contribution from the purely quartet pathway is quite small, being less than 16% for temperatures below 3000 K.

**3.2.4. Comparison with Experiment.** There have been a number of experimental studies of the  $\text{CH} + \text{N}_2$  reaction at high temperatures. In particular, Lindackers et al.,<sup>50</sup> Dean et al.,<sup>5</sup> and, most recently, Hanson and co-workers<sup>24</sup> have provided fairly direct studies of the kinetics for temperatures of 2000 K and higher. The last of these studies also examined the product distribution, concluding that  $\text{H} + \text{NCN}$  are the principal products, with a conservative lower bound to their branching ratio of 0.7. Meanwhile, Becker et al.<sup>51</sup> directly studied the kinetics in the 850–890 K range. A number of more indirect studies have also been presented.<sup>4,52–54</sup> Interestingly, a recent modeling study<sup>23</sup> has suggested that the rate to produce  $\text{NCN} + \text{H}$  must be 1–2 orders of magnitude greater than predicted by Moskaleva and Lin<sup>17</sup> to adequately predict flame species in low temperature flames (1000–1500 K).

In Figure 12, the present theoretical predictions for the rate coefficient are compared with the various experimental observations as well as the prior theoretical predictions of Moskaleva and Lin.<sup>17</sup> The present predictions are in remarkably good agreement with the very recent experimental measurements of Hanson and co-workers,<sup>24</sup> which in turn are representative of the body of high temperature experimental data. Furthermore,

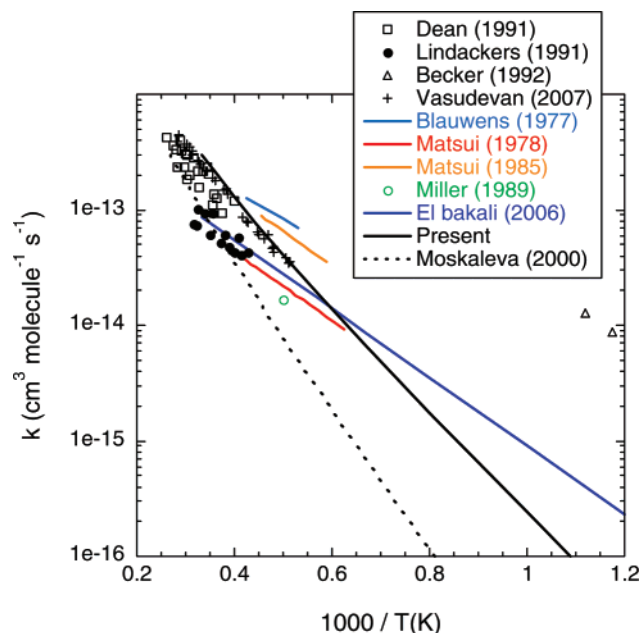


**Figure 12.** Plot of the experimental measurements and theoretical predictions for the CH + N<sub>2</sub> → NCN + H rate coefficient. The black symbols denote direct experimental results, the colored lines and symbols denote modeling results, while the black solid and dashed lines denote the theoretical predictions.

near the key temperature of 1500 K, the present predictions are in quantitative agreement with the best fit from the recent modeling study of El Bakali and co-workers<sup>23</sup> but do diverge somewhat toward lower temperatures. The experimental results of Becker et al.<sup>51</sup> in the 850–900 K range are 2 orders magnitude greater than the present predictions. This discrepancy may be indicative of the difficulty of disentangling the addition and bimolecular reaction rate coefficients at these temperatures.

The theoretical predictions of Moskaleva and Lin<sup>17</sup> are a factor of 5 lower than the theoretical and experimental results at 2000 K. Furthermore, the discrepancy between the two theoretical predictions increases with decreasing temperature, reaching a factor of 30 at 1000 K. It is unclear as to why the two theoretical predictions are so discordant. The difference of 2.0 kcal/mol in the H + NCN reaction endothermicity provides some explanation, but this should correlate with only a factor of 2.7 difference at 1000 K. The present VRC-TST treatment of the H + NCN channel should be much more accurate than the approach employed by Moskaleva and Lin. Nevertheless, a factor of 10 error and such a strong temperature dependence to the discrepancy is somewhat surprising. Notably, the present multireference treatment of TS<sub>3</sub> should actually yield a reduction in the rate coefficient because the barrier is higher and the entropy is lower.

It is perhaps worthwhile to consider the dominant sources of uncertainty in the theoretical predictions. The uncertainties in the TS<sub>3</sub> saddle point energy and in the H + NCN channel energy have the greatest effect on the kinetics since they are the two dominant bottlenecks. The effect of varying the TS<sub>3</sub> and H + NCN energies by ±2 kcal/mol is illustrated in Figure 13. These variations are more or less representative of the true uncertainties in the present theoretical estimates of these quantities. Note that a photodissociation study of Neumark and co-workers<sup>55</sup> estimated the NCN heat of formation (at 0 K) as 111.4 ± 0.7 kcal/mol, which implies a CH + N<sub>2</sub> → H + NCN reaction endothermicity of 21.2 ± 0.7 kcal/mol. The present theoretical estimate is 1.7 kcal/mol lower.

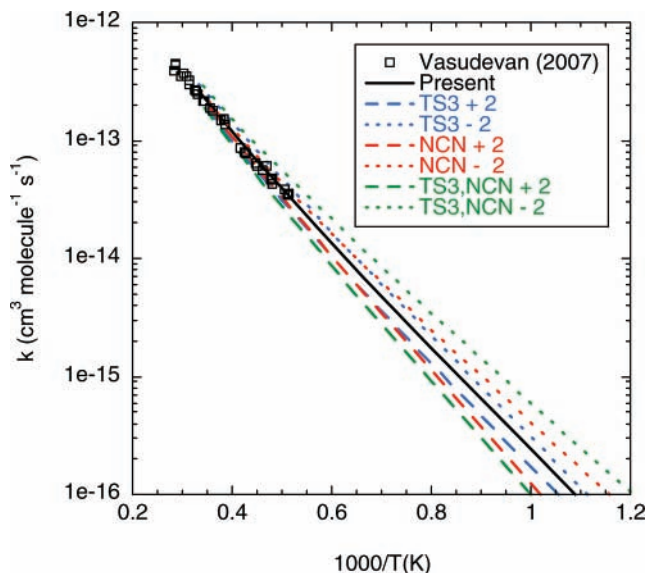


**Figure 13.** Plot of the sensitivity of the theoretical predictions for the CH + N<sub>2</sub> → NCN + H rate coefficient to the TS<sub>3</sub> and H + NCN energies. The blue, red, and green lines denote changes by ±2 kcal/mol of TS<sub>3</sub>, of H + NCN, or of both TS<sub>3</sub> and H + NCN, respectively.

The TS<sub>3</sub> variation changes the overall rate constant by a more or less constant factor of 1.25 over the 1000–3000 K range. In contrast, the variation in the H + NCN channel energy has a larger but more temperature-dependent effect; at 1000 K, it changes the rate by a factor of 1.7, while at 3000 K, it is only a 4% effect. This difference in behavior is related to the changing importance of the H + NCN and TS<sub>3</sub> transition states. The joint variation in both energies implies uncertainties in the present rate predictions of factors of 2.4, 1.4, and 1.2 at 1000, 2000, and 3000 K, respectively.

#### 4. Concluding Remarks

The present ab initio chemical kinetics predictions for the CH + N<sub>2</sub> → NCN + H rate coefficient are in quantitative agreement with the recent experimental measurements of Hanson and co-workers<sup>24</sup> for temperatures of 1940 K and higher. Furthermore, these predictions provide strong support for the magnitude of the rate constant proposed in the recent modeling study of El Bakali et al., at least near the practically important temperature of 1500 K.<sup>23</sup> The present predictions are well-reproduced over the 400–3000 K range by the modified Arrhenius form  $6.80 \times 10^{-16} T^{1.122} \exp(-8819/T)$  cm<sup>3</sup> molecule<sup>-1</sup> s<sup>-1</sup>, with  $T$  in Kelvin. These predictions are expected to be accurate to within about a factor of 2 for the practically important temperature range of 1000–2000 K. Accurate measurements of the heat of formation for NCN would greatly reduce the uncertainties in these predictions.

The application of multireference electronic structure methods was central to the resolution of the discrepancy between the recent experiments of Hanson and co-workers<sup>24</sup> and the prior theoretical results of Moskaleva and Lin.<sup>17</sup> The implementation of such multireference calculations within the VRC-TST approach was also a key component of the analysis, particularly at lower temperatures. At higher temperatures, TS<sub>3</sub>, the transition state for the formation of HNCN from its ring precursor, provides the dominant bottleneck. The HNHC pathway of Berman and co-workers<sup>25</sup> makes a significant contribution to the kinetics at higher temperatures. In contrast, the contribution of a purely quartet pathway is negligible, at least for temperatures below 3000 K.

**Acknowledgment.** This work was supported by the Division of Chemical Sciences, Geosciences, and Biosciences, the Office of Basic Energy Sciences, the U.S. Department of Energy. The work at Argonne was supported under DOE Contract DE-AC02-06CH11357. Sandia is a multiprogram laboratory operated by Sandia Corporation, a Lockheed Martin Company, for the United States Department of Energy under Contract DE-AC04-94-AL85000.

## References and Notes

- (1) Fenimore, C. P. *Proc. Combust. Inst.* **1971**, *13*, 373.
- (2) Hayhurst, A. N.; Vince, I. M. *Prog. Energy Combust. Sci.* **1980**, *6*, 35.
- (3) Miller, J. A. *Proc. Combust. Inst.* **1996**, *26*, 461.
- (4) Miller, J. A.; Bowman, C. T. *Prog. Energy Combust. Sci.* **1989**, *15*, 287.
- (5) Dean, A. J.; Hanson, R. K.; Bowman, C. T. *Proc. Combust. Inst.* **1991**, *23*, 259.
- (6) Lindackers, D.; Burmeister, M.; Roth, P. *Proc. Combust. Inst.* **1991**, *23*, 251.
- (7) Glarborg, P.; Miller, J. A.; Kee, R. J. *Combust. Flame* **1986**, *65*, 177.
- (8) Bair, R. A. *Annual Report*; Theoretical Chemistry Group (Chemistry Division), Argonne National Laboratory: Argonne, IL, September 1985.
- (9) Manaa, R. M.; Yarkony, D. R. *J. Chem. Phys.* **1991**, *95*, 1808.
- (10) Manaa, R. M.; Yarkony, D. R. *Chem. Phys. Lett.* **1992**, *188*, 352.
- (11) Martin, J. M. L.; Taylor, P. R. *Chem. Phys. Lett.* **1993**, *209*, 143.
- (12) Walch, S. P. *Chem. Phys. Lett.* **1993**, *208*, 214.
- (13) Miller, J. A.; Walch, S. P. *Int. J. Chem. Kinet.* **1997**, *29*, 253.
- (14) Rodgers, A. S.; Smith, G. P. *Chem. Phys. Lett.* **1996**, *253*, 313.
- (15) Miller, J. A.; Pilling, M. J.; Troe, J. *Proc. Combust. Inst.* **2005**, *30*, 43.
- (16) Cui, L.; Morokuma, K.; Bowman, J. M.; Klippenstein, S. J. *J. Chem. Phys.* **1999**, *110*, 9469.
- (17) Moskaleva, L. V.; Lin, M. C. *Proc. Combust. Inst.* **2000**, *28*, 2393.
- (18) Moskaleva, L. V.; Xia, W. S.; Lin, M. C. *Chem. Phys. Lett.* **2000**, *331*, 269.
- (19) Smith, G. P. *Chem. Phys. Lett.* **2003**, *367*, 541.
- (20) Bise, R. T.; Hoops, A. A.; Neumark, D. M. *J. Chem. Phys.* **2001**, *114*, 9000.
- (21) Szpunar, D. E.; Faulhaber, A. E.; Kautzman, K. E.; Crider, P. E., II; Neumark, D. M. *J. Chem. Phys.* **2007**, *126*, 114311.
- (22) Takayanagi, T. *Chem. Phys. Lett.* **2003**, *368*, 393.
- (23) El Bakali, A.; Pillier, L.; Desgroux, P.; Lefort, B.; Gasnot, L.; Pauwels, J. F.; da Costa, I. *Fuel* **2006**, *85*, 896.
- (24) Vasudevan, V.; Hanson, R. K.; Bowman, C. T.; Golden, D. M.; Davidson, D. F. *J. Phys. Chem. A* **2007**, in press.
- (25) Berman, M. R.; Tsuchiya, T.; Gregusova, A.; Perera, A.; Bartlett, R. J. *J. Phys. Chem. A* **2007**, *111*, 6894.
- (26) Dunning, T. H., Jr. *J. Chem. Phys.* **1989**, *90*, 1007.
- (27) Kendall, R. A.; Dunning, T. H., Jr.; Harrison, R. J. *J. Chem. Phys.* **1992**, *96*, 6796.
- (28) Woon, D. E.; Dunning, T. H., Jr. *J. Chem. Phys.* **1993**, *98*, 1358.
- (29) MOLPRO is a package of ab initio programs written by Werner, H.-J. and Knowles, P. J. with contributions from Almlöf, J.; Amos, R. D.; Berning, A.; Cooper, D. L.; Deegan, M. J. O.; Dobbyn, A. J.; Eckert, F.; Elbert, S. T.; Hampel, C.; Lindh, R.; Lloyd, A. W.; Meyer, W.; Nicklass, A.; Peterson, K.; Pitzer, R.; Stone, A. J.; Taylor, P. R.; Mura, M. E.; Pulay, P.; Schutz, M.; Stoll, H.; Thorsteinsson, T. The majority of calculations reported here was performed with version 2002.6.
- (30) Werner, H.-J.; Knowles, P. J. *J. Chem. Phys.* **1985**, *82*, 5053.
- (31) Knowles, P. J.; Werner, H.-J. *Chem. Phys. Lett.* **1985**, *115*, 259.
- (32) Celani, P.; Werner, H.-J. *J. Chem. Phys.* **2000**, *112*, 5546.
- (33) Werner, H.-J.; Knowles, P. J. *J. Chem. Phys.* **1988**, *89*, 5803.
- (34) Knowles, P. J.; Werner, H.-J. *Chem. Phys. Lett.* **1988**, *145*, 514.
- (35) Knowles, P. J.; Hampel, C.; Werner, H.-J. *J. Chem. Phys.* **1993**, *99*, 5219.
- (36) Frisch, M. J.; Trucks, G. W.; Schlegel, H. B.; Scuseria, G. E.; Robb, M. A.; Cheeseman, J. R.; Zakrzewski, V. G.; Petersson, G. A.; Montgomery, J. A., Jr.; Stratmann, R. E.; Burant, J. C.; Dapprich, S.; Millam, J. M.; Daniels, A. D.; Kudin, K. N.; Strain, M. C.; Farkas, O.; Tomasi, J.; Barone, V.; Cossi, M.; Cammi, R.; Mennucci, B.; Pomelli, C.; Adamo, C.; Clifford, S.; Ochterski, J.; Petersson, G. A.; Ayala, P. Y.; Cui, Q.; Morokuma, K.; Malick, D. K.; Rabuck, A. D.; Raghavachari, K.; Foresman, J. B.; Cioslowski, J.; Ortiz, J. V.; Stefanov, B. B.; Liu, G.; Liashenko, A.; Piskorz, P.; Komaroni, I.; Gomperts, R.; Martin, R. L.; Fox, D. J.; Keith, T. A.; Al-Laham, M. A.; Peng, C. Y.; Nanayakkara, A.; Gonzalez, C.; Challacombe, M.; Gill, P. M. W.; Johnson, B. G.; Chen, W.; Wong, M. W.; Andreas, J. L.; Head-Gordon, M.; Replogle, E. S.; Pople, J. A. *Gaussian 98*; Gaussian, Inc.: Pittsburgh, PA, 1998.
- (37) Martin, J. M. L.; Uzan, O. *Chem. Phys. Lett.* **1998**, *282*, 16.
- (38) Celani, P.; Werner, H.-J. *J. Chem. Phys.* **2003**, *119*, 5044.
- (39) Klippenstein, S. J. *J. Chem. Phys.* **1992**, *96*, 367.
- (40) Georgievskii, Y.; Klippenstein, S. J. *J. Chem. Phys.* **2003**, *118*, 5442.
- (41) Georgievskii, Y.; Klippenstein, S. J. *J. Phys. Chem. A* **2003**, *107*, 9776.
- (42) Harding, L. B.; Klippenstein, S. J.; Georgievskii, Y. *J. Phys. Chem. A* **2007**, *111*, 3789.
- (43) Harding, L. B.; Georgievskii, Y.; Klippenstein, S. J. *J. Phys. Chem. A* **2005**, *109*, 4646.
- (44) Berman, M. R.; Lin, M. C. *J. Phys. Chem.* **1983**, *87*, 3993.
- (45) Brownsword, R. A.; Herbert, L. B.; Smith, I. W. M.; Stewart, D. W. A. *J. Chem. Soc., Faraday Trans.* **1996**, *92*, 1087.
- (46) Fulle, D.; Hippler, H. *J. Chem. Phys.* **1996**, *105*, 5423.
- (47) Le Picard, S. D.; Canosa, A. *Geophys. Res. Lett.* **1998**, *25*, 485.
- (48) Hahn, D. K.; Klippenstein, S. J.; Miller, J. A. *Faraday Discuss.* **2001**, *119*, 79.
- (49) Lee, T. J.; Taylor, P. R. *Int. J. Quantum Chem.* **1989**, *S23*, 199.
- (50) Barlett, R. J.; Musial, M. *Rev. Mod. Phys.* **2007**, *79*, 291.
- (51) Lindackers, D.; Burmeister, M.; Roth, P. *Proc. Combust. Inst.* **1991**, *23*, 251.
- (52) Becker, K. H.; Engelhardt, B.; Geiger, H.; Kurtenbach, R.; Schrey, G.; Wiesen, P. *Chem. Phys. Lett.* **1992**, *195*, 322.
- (53) Blauwens, J.; Smets, B.; Peeters, J. *Proc. Combust. Inst.* **1977**, *16*, 1055.
- (54) Matsui, Y.; Yuuki, A. *Jpn. J. Appl. Phys.* **1985**, *24*, 598.
- (55) Matsui, Y.; Nomaguchi, N. *Combust. Flame* **1978**, *32*, 205.
- (56) Bise, R. T.; Choi, H.; Neumark, D. M. *J. Chem. Phys.* **1999**, *111*, 4923.